Spatially anisotropic $S = 1$ square-lattice antiferromagnet with single-ion anisotropy realized in a Ni(II) pyrazine-n, n'-dioxide coordination polymer

Jamie L. Manson [ORCID],[1,*] Daniel M. Pajerowski [ORCID],[2,†] Jeffrey M. Donovan,[1] Brendan Twamley,[3] Paul A. Goddard,[4,‡]
Roger Johnson,[5] Jesper Bendix,[6] John Singleton,[7] Tom Lancaster [ORCID],[8] Stephen J. Blundell,[9] Jacek Herbrych,[10]
Peter J. Baker [ORCID],[11] Andrew J. Steele [ORCID],[9] Francis L. Pratt,[11] Isabel Franke-Chaudet,[9] Ross D. McDonald,[7]
Alex Plonczak,[7] and Pascal Manuel[11]

[1]*Department of Chemistry, Biochemistry & Physics, Eastern Washington University, Cheney, Washington 99004, USA*
[2]*Neutron Scattering Division, Oak Ridge National Laboratory, Oak Ridge, Tennessee, USA*
[3]*University Research Office, University of Idaho, Moscow, Indiana 83844, USA*
[4]*Department of Physics, University of Warwick, Coventry CV4 7AL, United Kingdom*
[5]*Department of Physics and Astronomy, University College London, London, United Kingdom*
[6]*Department of Chemistry, University of Copenhagen, Copenhagen DK-2100, Denmark*
[7]*National High Magnetic Field Laboratory, Los Alamos National Laboratory, Los Alamos, New Mexico 87545, USA*
[8]*Department of Physics, Durham University, Durham DH1 3LE, United Kingdom*
[9]*Clarendon Laboratory, Department of Physics, University of Oxford, Oxford OX1 3PU, United Kingdom*
[10]*Department of Theoretical Physics, Wrocław University of Science and Technology, 50-370 Wrocław, Poland*
[11]*ISIS Facility, STFC Rutherford Appleton Laboratory, Didcot, Oxfordshire OX11 0QX, United Kingdom*

The Ni(NCS)$_2$(pyzdo)$_2$ coordination polymer is found to be an $S = 1$ spatially anisotropic square lattice with easy-axis single-ion anisotropy. This conclusion is based upon considering in concert the experimental probes x-ray diffraction, magnetic susceptibility, magnetic-field-dependent heat capacity, muon-spin relaxation, neutron diffraction, neutron spectroscopy, and pulsed-field magnetization. Long-range antiferromagnetic (AFM) order develops at $T_N = 18.5$ K. Although the samples are polycrystalline, there is an observable spin-flop transition and saturation of the magnetization at ≈ 80 T. Linear spin-wave theory yields spatially anisotropic exchanges within an AFM square lattice, $J_x = 0.235$ meV, $J_y = 2.014$ meV, and an easy-axis single-ion anisotropy $D = -1.622$ meV (after renormalization). The anisotropy of the exchanges is supported by density functional theory.

I. INTRODUCTION

Low-dimensional quantum magnetism continues to be an intensively studied research field, for both fundamental aspects of physics and potential technological implications [1]. Moreover, because of the multitude of different structures and connectivities provided by hybrid organic/inorganic compounds, it seems likely that molecule-based materials will play an important role in the future of electronic and magnetic devices. Understanding how different molecular ligands can be used to couple magnetic moments and underpin low-dimensional structures are important milestones along this road. Toward this end, we have studied a variety of coordination-polymer magnetic systems with different dimensionalities, exchange energies, and spin quantum numbers (see, e.g., Refs. [2–11]). Within the field of quantum magnets, the subfield of two-dimensional (2D) systems is attractive due to the ability to support long-range entangled states [12] and the analogies to theories of high-temperature superconductivity (HTSC). Historically, HTSC in copper compounds has pushed extensive research of $S = \frac{1}{2}$ materials, while the

discovery of iron-based HTSC has highlighted the need for $S = 1$ (and maybe larger) 2D quantum magnets to be studied in that context [13]. The extension to $S = 1$ allows the usual three dipolar operators and dipolar magnetic ordering (as in $S = \frac{1}{2}$) but adds the complexity of five additional quadrupolar operators and respective magnetic order parameters [14]. Recently, advances in neutron scattering data acquisition and modeling have shown the quantitative effects of quadrupolar excitations in the triangular lattice $S = 1$ material FeI$_2$ [15].

Here, we consider a Hamiltonian of the spatially anisotropic $S = 1$ antiferromagnet (AFM) on a square lattice with single-ion anisotropy. Typically, this equation is written as

$$H = J_x \sum_{\langle i,j \rangle_x} \mathbf{S}_i \cdot \mathbf{S}_j + J_y \sum_{\langle i,j \rangle_y} \mathbf{S}_i \cdot \mathbf{S}_j + D \sum_i S_{iz}^2, \quad (1)$$

where the first sum is along the x direction of the square lattice having exchange energy J_x, the second sum along the y direction with exchange energy J_y, angle brackets denote nearest-neighbor summations, and D is the single-ion anisotropy. There are often 1 subscripts on J_x and J_y, as a common addition to this Hamiltonian is diagonal exchange within the square (J_2), which is frustrating with respect to J_1 [13]. In the limit that J_x or J_y is zero and D is zero, then Eq. (1) reduces to uncoupled $S = 1$ isotropic spin chains that have a gapped

ground state called the Haldane phase [16–18]. The parameter $\alpha = J_x/J_y$ is often introduced as a notational convenience. Then this Haldane phase has a region of stability in the phase space of α and D/J_y [19]. In the $D = 0$ limit, a small but finite coupling (e.g., $\alpha \approx 0.04$) between chains induces a quantum phase transition from the Haldane phase to a long-range ordered AFM phase [19–21]. Jointly considering D and α shows that both parameters are destabilizing with respect to the Haldane phase, either toward long-range magnetic order or quantum paramagnetism. The parameter $J_{2d} = \frac{1}{2}(J_x + J_y)$ is used in cases where the effect of spatially anisotropic exchange is undeterminable, and $J_x = \frac{2\alpha}{(1+\alpha)}J_{2d}$ and $J_y = \frac{2}{(1+\alpha)}J_{2d}$. Finally, sufficiently large easy-plane anisotropy introduces a quantum paramagnetic phase that has no dipolar order but instead a quadrupolar order parameter $\langle S_z^2 - \frac{2}{3} \rangle$.

Experimentally, coordination-polymer chemistry has been foundational to provide real systems that obey Eq. (1). There is a synergistic relationship between the parallel maturity of magnetochemistry and the many-body physics that describes low-dimensional quantum magnets. While the state of the art does not yet allow deterministic crystal engineering to connect synthesis to the resultant magnetism Hamiltonian, in some cases, the ever-growing library of compounds allows for increasing control of parameters like D and J from the constituent ligands and ions of compounds. An example of this connection is in our work on $S = 1$ Ni(II) coordination polymers [8]. We have been engaged in the detailed study of $S = \frac{1}{2}$ and 1 quantum magnets based on polymeric 2D $[M(\text{pyz})_2]^{2+}$ ($M = $ Cu or Ni) square grids [2,5,22]. The geometry of these grids may be perfectly square (due to tetragonal in-plane symmetry) or bear some rhombic distortion by imposing $M \cdots M$ edges of slightly different lengths and/or metal-ligand bond angles appreciably more or less than 90°.

Among metal-organic compounds, Cu(II) square-lattice coordination polymers are the most known and the best characterized. However, the library of related $S = 1$ Ni(II) compounds is far less populated, and the ability to grow suitable single crystals for detailed investigation is challenging. Unlike octahedral Cu(II) complexes where the single magnetic electron usually resides in the $d_{x^2-y^2}$ orbital, octahedral Ni(II) has unpaired electron density distributed in both $d_{x^2-y^2}$ and d_{z^2} orbitals. In addition, Cu(II) is Jahn-Teller active, while such a distortion does not occur in Ni(II) systems. The impact of the difference in electronic structure tends toward stronger magnetic couplings exhibited by Cu(II) coordination compounds than Ni(II) irrespective of the organic bridging ligands, such as pyrazine (pyz).

Pyrazine may be the most utilized bridging ligand in coordination chemistry applications, while its dioxide, namely, pyrazine-n, n'-dioxide (hereafter pyzdo), is less explored, although a few notable examples exist such as Cu$X_2(\text{H}_2\text{O})_2(\text{pyzdo})$ ($X = $ Cl, Br) [23], Co $(\text{dca})_2(\text{pyzdo})$ (dca = dicyanamide) [24], and Mn(NCS)$_2$(pyzdo)$_2$ [25]. In this paper, we have combined Ni(II) ions with pyzdo ligands to afford the 2D coordination polymer Ni(NCS)$_2$(pyzdo)$_2$ that is isostructural to the Mn(II) and Co(II) analogs [25]. The magnetometry data of Mn(NCS)$_2$(pyzdo)$_2$ and Co(NCS)$_2$(pyzdo)$_2$ are consistent with high 2D magnetism, suggesting that Ni(NCS)$_2$(pyzdo)$_2$ is likely to obey Eq. (1).

Thus, Ni(NCS)$_2$(pyzdo)$_2$ adds to the small library of experimental realizations of spatially anisotropic $S = 1$ square-lattice AFMs with single-ion anisotropy. Aside from the aforementioned NiX_2(pyz)$_2$ compounds [5] (of which NiBr$_2$(pyz)$_2$ was reported before [26]), we have also found a recent report on Ni[SC(NH$_2$)$_2$]$_6$Br$_2$ [27], which was shown to have long-range AFM order at $T_N = 2.23$ K, and magnetization data showed a strong magnetic anisotropy, although details of the Hamiltonian parameters are yet to be determined.

II. RESULTS AND DISCUSSION

Here, we subjected Ni(NCS)$_2$(pyzdo)$_2$ to a variety of experimental probes and theoretical models with the goal of quantitatively determining the Hamiltonian. We begin in Sec. II A by presenting x-ray diffraction to determine the crystal structure. Section II B presents the temperature-dependent magnetic susceptibility data, from which the system appears AFM and highly 2D with $J_{2d} = 13.4$ K (1.15 meV) and $T_N \approx 18$ K. Heat capacity measurements in zero field are reported in Sec. II C and show a clear peak at $T_N = 18.5$ K that decreases in temperature with applied magnetic field consistent with AFM. Muon-spin relaxation (Sec. II D) further corroborates these results. Section II E presents neutron diffraction data, which show the magnetic structure is an AFM square-lattice with moments (≈ 1.8 μ_B per nickel) approximately along the putative easy axis of the NiN$_2$O$_4$ moieties. Plane-wave density functional theory (DFT, Sec. II F) sets the stage for considerations of magnetic exchange and upholds the emerging picture of a spatially anisotropic square lattice. Section II G contains neutron spectroscopy data on a polycrystalline sample, which are quantitatively modeled with linear spin-wave theory (LSWT) by a spatially anisotropic square lattice ($J_x = 0.235$ meV, $J_y = 2.014$ meV) having an easy-axis single-ion anisotropy ($D = -0.811$ meV, renormalized to -1.622 meV in the low-temperature limit beyond the approximation of LSWT). Some theoretical modeling is discussed in Sec. II H, and Sec. II I discusses pulsed-field magnetization data on a polycrystalline sample. The latter show quantitative agreement with the saturation field of the spectroscopy-derived Hamiltonian ($\mu_0 H_{\text{SAT}} \approx 80$ T) and qualitative agreement of the magnetizing curve, considering a mean-field model. Density matrix renormalization group (DMRG) theory is also compared with magnetization and neutron spectroscopy, giving highly similar but quantitatively different Hamiltonian parameters. Dimer-cluster DFT is presented in Sec. II J, which shows how the same pyzdo ligand can yield an order of magnitude difference in exchange energies due to modifications of the connecting geometry. Additional considerations are discussed in Sec. III, and the main conclusions are summarized in Sec. IV. Experimental details that are not present in the main body of the text are available in Appendix.

A. X-ray diffraction

Single-crystal x-ray diffraction was used to determine the crystal structure of Ni(NCS)$_2$(pyzdo)$_2$ at 90 K, and this compound is isomorphous to the Mn- and Co-analogs reported several years ago [25]. The crystallographic information file
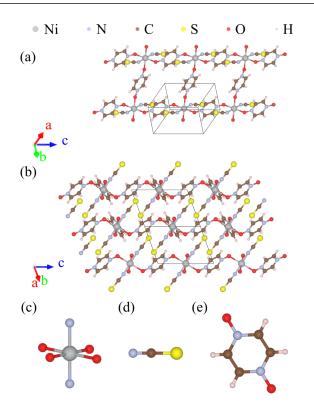
FIG. 1. Crystal structure of Ni(NCS)$_2$(pyzdo)$_2$. (a) A section of one layer of nickel ions bridged by pyzdo ligands. (b) Stacking of the layers. Molecular units of (c) NiO$_4$N$_2$ octahedra, (d) NCS, and (e) pyzdo.

FIG. 2. Magnetic susceptibility of Ni(NCS)$_2$(pyzdo)$_2$ measured in 0.1 T. (a) Data and Lines [29] model fit described in the text. (b) Inverse susceptibility data and Curie-Weiss law fit described in the text. (c) Product of susceptibility and temperature with derivative inset.

(CIF) is available in the Supplemental Material [28]. These data are presented first, as knowledge of the crystal structure is foundational to considering the magnetic properties. Each Ni(II) ion resides on an inversion center and is equatorially co-ordinated to O-donor atoms from four different pyzdo ligands at distances of 2.101(1) and 2.104(1) Å. The axial positions are occupied by N donors from the NCS$^-$ anion, and each NiO$_4$N$_2$ octahedron is slightly compressed along this direction. The octahedra are rhombically distorted away from ideal D_{4h} symmetry, with the largest deviation being 86.81(6)°.

Bridging pyzdo ligands connect NiO$_4$N$_2$ octahedra into 2D arrays of tiled parallelograms defined by [1, −1, 0] and [0, 0, 1] real space directions, Fig. 1(a). These 2D arrays propagate along the [1,1,0] direction, Fig. 1(b), and are staggered to maximize interlayer van der Waals contacts. Molecular units of Ni(NCS)$_2$(pyzdo)$_2$ are shown in Figs. 1(c)–1(e). Within each 2D layer, adjacent octahedra adopt the same configuration and are tilted in accord with the nonlinear Ni–O–N bond angles of 115.3(1)° and 120.9(1)° for Ni1-O5-N6 and Ni-O1-N2, respectively. Also noticeable is the interdigitation of the protruding NCS$^-$ anions which themselves are nearly linear [178.8(2)°]. Weak electrostatic interactions comprised of N–O⋯H hydrogen bonds exist and help hold the layers together.

B. Magnetic susceptibility

Magnetic susceptibility (χ) for polycrystalline samples is sensitive to magnetic interactions and less so to single-ion anisotropy. This low-field magnetic response is sensitive
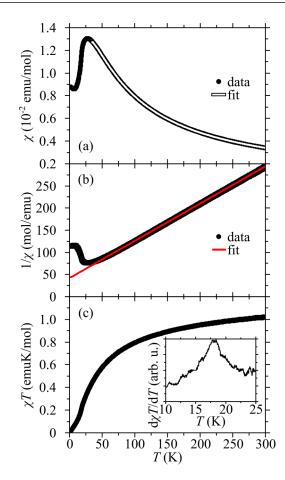
to the onset of long-range magnetic order and to magnetic correlations in the sample and allows comparison with quantitative models of the superexchange. The $\chi(T)$ data for Ni(NCS)$_2$(pyzdo)$_2$ as measured in a 0.1 T field are shown in Fig. 2(a). A broad maximum is identified at $T_{max} = 28$ K, where $\chi(T)$ takes the value of 0.013 emu/mol. Below T_{max}, $\chi(T)$ decreases to reach a minimum value of 0.009 emu/mol at a base temperature of 2 K. The broad maximum signifies the presence of short-range spin correlations, which may be 2D, as suggested by the crystal structure. The T_{max} value was used to estimate the intralayer exchange constant ($H_{Lines} = J_{2d} \sum_{\langle i,j \rangle} \mathbf{S}_i \cdot \mathbf{S}_j$) for a 2D AFM without single-ion anisotropy from the equation developed by Lines [29] for any value of S and $J_{2d} > 0$, $T_{max}/J = 1.12S(S+1) + 0.1$, which yields $J_{2d} \approx 12$ K (1.0 meV) for $S = 1$. The $\chi(T)$ data >30 K were fit to the Lines model of susceptibility, and the resulting fit is shown as the solid line in Fig. 2(a). Excellent agreement between the data and fit were obtained for the parameters $g = 2.091(1)$, $J_{2d} = 13.35(1)$ K (1.15 meV), and TIP = 220(6)×10^{-6} emu/mol. Here, g is the Landé g factor, and TIP is temperature-independent paramagnetism. In accord with the Lines model, a positive J value indicates an AFM interaction. Inclusion of an interlayer magnetic coupling based on the mean-field approximation with z magnetic
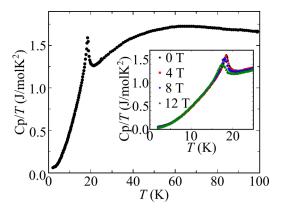
FIG. 3. $Ni(NCS)_2(pyzdo)_2$ heat capacity. Heat capacity divided by temperature with the magnetic field dependence inset.

neighbors led to a small ferromagnetic (FM) zJ' value of $-0.009(1)$ K (-8×10^{-4} meV) which further supports a high degree of isolation between the 2D magnetic layers.

The reciprocal magnetic susceptibility $1/\chi$ vs T is shown in Fig. 2(b), and these data were fitted to a Curie-Weiss law ($\chi = \frac{Ng^2\mu_B^2}{3k_B(T+\theta_{CW})}S[S+1]$) between 80 and 300 K, where k_B is Boltzmann's constant, μ_B is the Bohr magneton, and θ_{CW} is the Weiss temperature. Good agreement was achieved for $g = 2.121(1)$ and $\theta_{CW} = -49.78(1)$ K. The g factor is typical of Ni(II), whereas the large and negative Weiss constants are an indication for significant AFM interactions between $S = 1$ Ni(II) ions.

The temperature variation of χT is displayed in the main plot of Fig. 2(c) with the low-T portion of $d\chi T/dT$ vs T highlighted in the inset. Upon cooling from room temperature, χT decreases smoothly until ~ 50 K, where it decreases more quickly. An abrupt change in the curvature of χT occurs ~ 18 K, which coincides with a peak in $d(\chi T)/dT$. We ascribe this anomaly to the transition to long-range AFM order in $Ni(NCS)_2(pyzdo)_2$. In the molecular field approximation, the Néel temperature $T_N = \theta_{CW}$, and the large discrepancy between the two supports the conjecture of $Ni(NCS)_2(pyzdo)_2$ as low dimensional. In general, deviations from $T_N = \theta_{CW}$ can be assigned to fluctuations beyond the molecular field approximation, which may be due to low dimensionality (as here) or magnetic frustration.

C. Heat capacity

Measuring heat capacity (C_p) as a function of temperature provides direct insight into the thermodynamics of materials. Here, for $Ni(NCS)_2(pyzdo)_2$, C_p is a direct probe of the phase transition from a paramagnetic to long-range ordered magnetic state. Application of external magnetic field further allows the discernment of magnetic interactions, e.g., the mean sign of the superexchanges. Polycrystalline measurements are presented as a function of magnetic field, Fig. 3. In zero field, data were collected from 2 to 100 K, and a sharp peak is observed at $T_N = 18.5$ K. Field-dependent data were collected from 2 to 25 K, and the peak shifts to lower temperatures and broadens with increasing applied magnetic field due to dominant AFM interactions. The broadening of the peak with increasing field is likely due to the polycrystalline
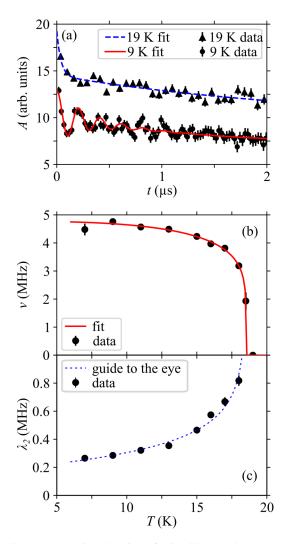

FIG. 4. Muon-spin relaxation of $Ni(NCS)_2(pyzdo)_2$. (a) Example asymmetry spectra, $A(t)$, measured at 9 K and 19 K. The 9 K data are shown in percent; the 19 K data have been displaced upward by 4% for clarity. (b) Temperature dependence of the muon precession frequency. (c) Relaxation rate as a function of temperature. In (c), the line is a guide to the eye.

sample having all orientations of applied field with respect to single-ion anisotropy.

D. Muon-spin relaxation

Muon-spin relaxation (μ^+SR) measurements are sensitive to local magnetic fields in a sample that provide information about magnetic correlations. In the preceding text, the paramagnetic-to-AFM phase transition in $Ni(NCS)_2(pyzdo)_2$ was identified, but muons probe the local correlations that are more directly connected to the sublattice magnetization and provide additional evidence to the evolving picture of the phase transition. Zero-field μ^+SR data were measured for a $Ni(NCS)_2(pyzdo)_2$ polycrystalline sample. Typical spectra measured above and below the transition temperature are shown in Fig. 4(a). Data measured at 18.5 K and below were fitted to an asymmetry function of the form:

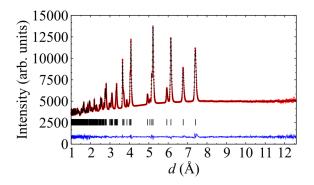$$A(t) = A_1 \cos(2\pi \nu t + \phi)e^{-\lambda_1 t} + A_2 e^{-\lambda_2 t}, \quad (2)$$

FIG. 5. Neutron diffraction of $Ni(NCS)_2(pyzdo)_2$ at $T = 25$ K in the paramagnetic state. Data are red circles, the model is a black line, vertical marks are Bragg peak positions, and residuals are an offset blue line.

where the first and second terms represent a damped oscillation and a pure relaxation, respectively [2]. The oscillations reflect the coherent precession of muon spins about a local magnetic **B** field, consistent with this field being similar at each muon stopping site, implying that the system is in an ordered magnetic state throughout the bulk. The purely relaxing component represents those muons whose spins are parallel to the local field and thus do not precess. The exponential relaxation is caused by the gradual depolarization of the muons due to dynamic processes and field inhomogeneities. Data measured at 19 K and above are purely relaxing and display no visible oscillation, such that they are not well described by (the first term of) Eq. (2).

The precession frequencies ν and relaxation rates λ_2 obtained from fitting are plotted against T, Fig. 4(b). The observed trends are consistent with the phase transition in $Ni(NCS)_2(pyzdo)_2$, with the relaxation rate diverging and the frequency acting as an effective order parameter. To model the transition, the muon precession frequency was fitted to a simple phenomenological model $\nu(T) = \nu(0)[1 - (\frac{T}{T_N})^{a_1}]^{a_2}$ [30] giving a critical temperature $T_N = 18.6 \pm 0.1$ K. This critical temperature is identical, within uncertainty, to that determined by magnetic susceptibility and heat capacity. Insufficient data are available for the a_1 and a_2 parameters to provide quantitative information about the critical behavior.

E. Neutron diffraction

Neutron scattering has different radiation interactions with materials than x-ray scattering, which provides greater sensitivity to lighter elements (e.g., H, N, O), and magnetic diffraction intensities are of a comparable order of magnitude to those from nuclear scattering. Up to this point, $Ni(NCS)_2(pyzdo)_2$ was shown to have AFM correlations from the magnetic susceptibility and heat capacity. Magnetic neutron diffraction allows quantitative extraction of the magnetic structure, which is the first step in quantitatively modeling the underlying magnetic Hamiltonian. Data collected at $T = 25$ K above the onset of long-range magnetic order were used to fit the nuclear crystal structure of $Ni(NCS)_2(pyzdo)_2$. The $T = 25$ K diffractogram shows sharp Bragg peaks, Fig. 5, which are modeled well by the x-ray crystal structure and allowed further refinement of the H and O positions as well as the variation of the crystallographic unit cell parameters expected

TABLE I. Neutron diffraction model parameters for $T = 25$ K.

Lattice	
Space group	P-1
a (Å)	6.8533(1)
b (Å)	7.0173(2)
c (Å)	8.0189(2)
α (°)	82.720(3)
β (°)	67.077(2)
γ (°)	74.315(1)
Atomic fractional coordinates	
H3	0.834(1), 0.329(1), 0.072(1)
H4	0.176(1), 0.496(1), 0.217(1)
H7	0.715(1), 0.088(2), 0.375(2)
H8	1.136(2), 0.276(1), 0.553(1)
O1	0.4622(9), 0.3244(9), 0.3224(9)
O5	0.829(1), 0.3802(8), 0.4271(8)
Refinement	
Rw (%)	1.06
Rbragg (%)	1.92

on cooling, Table I. This nuclear structure is available as a CIF in the Supplemental Material [28].

Deep within the magnetically ordered state at $T = 1.5$ K, new Bragg peaks appear that are due to the magnetic order, Fig. 6. Results of modeling the $T = 1.5$ K neutron diffraction are summarized in Table II. The propagation vector $k = (\frac{1}{2}, 0, \frac{1}{2})$ corresponds to a magnetic structure in which nearest-neighbor nickel ions connected by O-pyz-O
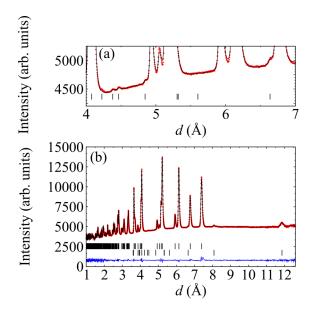

FIG. 6. Neutron diffraction of $Ni(NCS)_2(pyzdo)_2$ at $T = 1.5$ K in the magnetically ordered state. Data are red circles, the model is a black line, vertical marks are Bragg peak positions, and residuals are an offset blue line. Data are shown over (a) a region of interest that highlights the magnetic Bragg peaks and vertical marks for magnetic Bragg peak locations and (b) a large range of d spacing with upper vertical marks for structural Bragg peaks and lower vertical marks for magnetic Bragg peaks.

TABLE II. Neutron diffraction model parameters for $T = 1.5$ K.

Lattice	
Space group	P-1
a (Å)	6.8527(1)
b (Å)	7.0164(1)
c (Å)	8.0183(2)
α (°)	82.734(2)
β (°)	67.078(2)
γ (°)	74.318(1)
Propagation vector	
k	$(\frac{1}{2}, 0, \frac{1}{2})$
Ni magnetic moment	
$\|M\|$ (μ_B)	1.8(1)
θ(°)	−41(10)
φ(°)	67(12)
Refinement	
Rw (%)	1.03
Rbragg (%)	2.11
Rmag (%)	2.70

ligands form a distorted AFM square lattice (Fig. 7) in a plane containing direct lattice vectors [1, −1, 0] and [0, 0, 1]. Nearest-neighbor magnetic moments along a (6.8527 Å) are antiparallel, and nearest-neighbor magnetic moments along b (7.0164 Å) are parallel. By symmetry, the nickel moment for a given unit cell may point along any direction and refines to be approximately perpendicular to the NiO$_4$ plane, i.e., the moment direction is consistent with the NiN$_2$O$_4$ octahedra having an easy-axis anisotropy. Quantitatively, the moment orientation reported in spherical coordinates is $\theta = -41(10)°$ and $\varphi = 67(12)°$, where $x = \sin\theta\cos\varphi$, $y = \sin\theta\sin\varphi$, and $z = \cos\theta$, defined with x parallel to a, y perpendicular to a and in the ab plane, and $z = x \times y$. The surface normal to NiO$_4$ has $\theta = -43.5°$ and $\varphi = 81.9°$, and the line parallel to the Ni-N bond has $\theta = -46.1°$ and $\varphi = 77.1°$. This magnetic structure is available as an mCIF in the Supplemental Material [28].

The temperature dependence of the ordered moment is shown in Fig. 8. These data are fit to the equation
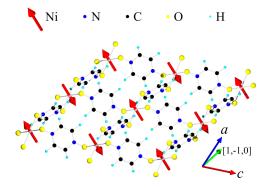

FIG. 7. Visualization of magnetic structure from neutron diffraction of Ni(NCS)$_2$(pyzdo)$_2$. This image shows a section of one layer of nickel ions bridged by pyzdo ligands overlayed with magnetic moment vectors.
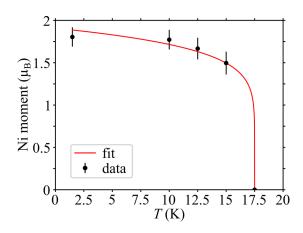

FIG. 8. Ordered magnetic moment vs temperature from neutron diffraction for Ni(NCS)$_2$(pyzdo)$_2$. Uncertainties are from counting statistics.

$m(T) = m(0)[1 - (\frac{T}{T_N})]^\beta$ with the β exponent fixed to the 2D Ising value of $\frac{1}{8}$ [31], $m(0) = 1.8(1)$ μ_B, and $T_N = 17.5$ K, which is where the magnetic diffraction intensities became zero. The discrepancy between this transition temperature and that of the other probes may be due to thermal gradients between the thermometer and the sample. Thus, while there is unquantifiable experimental uncertainty in this neutron-diffraction-determined transition temperature, it is still useful to show approximate agreement to the more finely sampled-in-temperature measurements (e.g., the heat capacity).

F. Plane-wave DFT

Plane-wave DFT was used to calculate the relative energies of different magnetic structures while using the experimentally determined nuclear crystal structure. These DFT energies can then be used to calculate the Heisenberg model superexchanges. For insulators like Ni(NCS)$_2$(pyzdo)$_2$, plane-wave DFT has been shown to capture the relative magnitude of superexchanges and, with appropriate parameterization, can provide quantitative descriptions of the magnetism. Looking forward to modeling the magnetic correlations with neutron spectroscopy, having a motivated starting point in the model optimization for the superexchanges is invaluable in achieving a good solution. Upon initial inspection of the (magnetic) crystal structure, Ni(NCS)$_2$(pyzdo)$_2$ seems to be a realization of an AFM square lattice, but these calculations provide the first illustration of the highly spatially anisotropic superexchanges present and the dominance of the in-plane superexchanges.

While the primitive unit cell of Ni(NCS)$_2$(pyzdo)$_2$ has one nickel ion, doubling along each crystallographic direction gives a supercell with eight nickel ions, Fig. 9(a). This larger unit cell is useful for calculating magnetic interactions. The five nearest nickel-nickel distances were considered as potential superexchange pathways, Fig. 9(a). These superexchange pathways were used to write down a Heisenberg superexchange Hamiltonian ($H = \sum_{\langle i,j \rangle} J_{ij} \mathbf{S}_i \cdot \mathbf{S}_j$) for nearest neighbors. Eight different magnetic structures were considered, and the energies of the different configurations were fit to the nearest-neighbor superexchange Hamiltonian model,
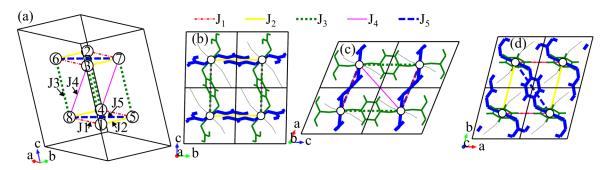
FIG. 9. Superexchange pathways in Ni(NCS)$_2$(pyzdo)$_2$. (a) The $2 \times 2 \times 2$ unit cell containing 8 nickel atoms as white circles with numbered labels for the density functional theory (DFT) magnetic structure calculations. Views along (b) a axis, (c) b axis, and (d) c axis are shown with only nickel atoms shown as white circles but with all atom-atom bonds shown. The thick blue solid line pyzdo connections are along the J_5 superexchange, the medium thickness green solid line pyzdo connections are along the J_3 superexchange, and the NCS bonds are thin gray solid lines. For (b)–(d), individual unit cells within the $2 \times 2 \times 2$ unit cell are shown.

Table III. The E_{VASP} parameters are taken directly from the VASP optimizer, with energies relative to the ↑↑↓↓↑↑↓↓ configuration. Using the Heisenberg superexchange Hamiltonian, a configuration energy may be generated as a function of the considered superexchanges (J_1, J_2, J_3, J_4, and J_5), which numerically evaluates to E_{fit}. Then a least-squares optimization of the superexchanges is performed by comparing E_{VASP} and E_{fit} for all configurations calculated. These superexchange energies associated with the plane-wave DFT Heisenberg model are shown in Table IV. The two largest superexchange values (J_3 and J_5) are along the bridging pyzdo molecules, as illustrated in Figs. 9(b)–9(d). The J_3 superexchange is more than five times greater than the J_5 superexchange, and the strength of the interaction anticorrelates to the nickel-to-nickel distance of 8.08 vs 8.38 Å. While the total distance for the J_3 vs J_5 pathway changes substantially by 0.3 Å, the changes in interatomic distances for the bridge are 100 times less (relatively almost no change). Therefore, the constituent molecules are well approximated as rigid bodies, and the bridge distance change is accommodated by the Ni-O-N angle that increases from 115.25° to 120.91°. Relating these calculations back to the spatially anisotropic square lattice of Eq. (1), $J_3 = J_y$ and $J_5 = J_x$. While these calculations do not consider the on-site direction of the magnetic moments, the sign changes from site to site for the ground-state configuration are consistent with the experimentally determined magnetic structure from the neutron diffraction experiments.

TABLE III. DFT energies and nearest-neighbor model energies for Ni(NCS)$_2$(pyzdo)$_2$. The list of up and down arrows defines the relative magnetic configurations, with the ordered mapping as in Fig. 9(a).

Configuration	E_{fit} (meV)	E_{VASP} (meV)	$E_{\text{VASP}} - E_{\text{fit}}$ (meV)
↑↑↓↓↑↑↓↓	–	0	–
↑↑↑↑↑↑↑↑	78.388	78.568	−0.180
↑↓↑↑↓↑↓↑↓	66.319	66.147	0.172
↑↑↑↑↓↓↓↓	78.028	78.199	−0.172
↑↓↓↑↑↑↓↓↑	11.934	11.755	0.179
↑↓↓↑↓↑↑↑↓	11.708	11.537	0.171
↑↑↓↓↓↓↑↑	0.606	0.785	−0.179
↑↓↑↓↓↑↓↑	67.060	66.880	0.180

G. Neutron spectroscopy

The differential scattering cross-section of inelastic neutron scattering is directly related to time and space pair correlation functions, such as those due to magnons in a long-range ordered magnet. Practically, neutron spectroscopy allows for extraction of Hamiltonian parameters. With the stage set for Ni(NCS)$_2$(pyzdo)$_2$ by the observations of the magnetic phase transition, knowledge of the magnetic structure, and DFT estimates of the superexchanges, the neutron spectroscopy problem is well posed. The correlations in Ni(NCS)$_2$(pyzdo)$_2$ are compared for temperatures above and below the onset of long-range magnetic order. Spectra at temperatures of $T = 2$ K (below T_N) and $T = 22$ K (above T_N) were measured with incident energies (Ei's) of 1.55, 3.32, 6.59, 12, and 25 meV. The preponderance of magnetic scattering was found to be contained in the $Ei = 12$ meV data, as shown by subtracting the $T = 22$ K spectrum from the $T = 2$ K spectrum, as in Fig. 10. The feature ~ 2 meV is an instrumental artifact from multiple scattering. The other inflections in the $T = 22$ K data are associated with lattice vibrations in the sample. The oversubtraction giving rise to negative intensity in the $I(2 \text{ K})$–$I(22 \text{ K})$ data is due to (presumably short-range) magnetic correlations persisting above the Néel temperature.

The Hamiltonian used to analyze these data is

$$H = \sum_{\langle i,j \rangle} J_{ij} \mathbf{S}_i \cdot \mathbf{S}_j + D \sum_i S_{iz}^2, \qquad (3)$$

where the exchange energies (J) are positive for AFM, the local easy axis (z coordinate) is along the direction determined from neutron diffraction, and the single-ion anisotropy energy (D) is negative for an easy axis.

Using LSWT, four models of the observed spin waves in Ni(NCS)$_2$(pyzdo)$_2$ were refined, Fig. 10. Although powder data, there are clear observables that may be related to a LSWT model. For example, in a 2D AFM with D/J_{2d} small, the bandwidth is $\approx 2|J_{2d}|$, and the gap in the excitation spectrum is $\approx 4\sqrt{|J_{2d}||D|}$. Visually, the powder spectrum ranges from ≈ 4 to ≈ 6.5 meV, so quickly one may estimate $|J_{2d}| \approx 1.25$ meV, and single-ion anisotropy must be easy axis to create the large gap, so $|D| \approx 0.9$ meV. The presented models have three extrinsic parameters: a constant background,

TABLE IV. Model superexchange values and definitions from plane-wave DFT for $Ni(NCS)_2(pyzdo)_2$. (positive J is AFM).

Index	Distance (Å)	Direction vector	Lattice direction	Orientation from magnetic structure	J_{VASP} (meV)
J_1	6.87	1,0,0	a	AFM	0.031
J_2	7.04	0,1,0	b	FM	−0.013
J_3	8.08	0,0,1	c	AFM	4.150
J_4	8.29	−1, 0, 1	$-a$, c	FM	0.005
J_5	8.38	1, −1, 0	a, $-b$	AFM	0.719

a linear background, and an overall scale factor. In model 1, there are two intrinsic parameters: the single-ion anisotropy (D) and a scaling factor of the superexchange values from DFT in Table IV. Model 1 captures all the qualitative features of the data, and the Hamiltonian parameters are shown in Table V. However, the ratio of J_3 to J_5 seems off, as it dictates the distance between the peaks in the magnon density of states at ≈5 and ≈6 meV, which also looks to underestimate the gap and D due to most weight of the fit being to the ≈6 meV peak. Therefore, a second model (model 2) was refined with three intrinsic parameters (D, J_3, and J_5) and with $J_1 = J_2 = J_4 = 0$, corresponding to the titular spatially anisotropic square lattice ($0 < \alpha < 1$) with single-ion anisotropy. This second model shows a 50% reduction in the residuals of the fit, with small modifications to the superexchange parameters. A third model (model 3) with two intrinsic parameters (D and J) that forces $J_3 = J_5$ as in a formally square lattice ($\alpha = 1$) was refined to give a poorer fit due to a lack of the van Hove singularity to give a peak in the magnon density of states at ≈5 meV. Finally, a fourth model (model 4) in which the interchain interactions are infinitesimally small ($\alpha = 0$, as a spin chain) also has two intrinsic parameters (D and J), where $J = J_3$, and all other exchanges are zero. The spin-chain model 4 performs better than the square-lattice model but not as well as the spatially anisotropic square-lattice model 2. For LSWT, the single-ion anisotropy acts identically to a staggered field, and comparing models 2 and 4 shows how
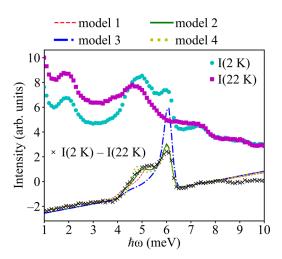
this spatially anisotropic square-lattice may be approximated by a spin chain for the dominant exchange in a static mean field of the weaker exchange: $|D(\text{model } 4)| \approx |D(\text{model } 3)| + |J_5(\text{model } 3)|$ and $J_3(\text{model } 4) \approx J_3(\text{model } 3)$. The LSWT parameters of these models are shown in Table V.

To better illustrate the LSWT models, a plot without powder averaging is shown in Fig. 11. This plot uses the $2 \times 2 \times 2$ unit cell of Fig. 9(a). All models are gapped due to the single-ion anisotropy breaking the rotational symmetry of the ground state. For the isotropic square lattice of model 3 with only one superexchange, there is intensity piling up at ≈6 meV when powder averaging due to many states being present at the top of the band. For the spatially anisotropic square lattices of models 1 and 2, there is a second component causing the intensity to also pile up at ≈5 meV. The additional exchanges of model 1 vs model 2 cause the additional inflections apparent in Fig. 10 due to further mode modulation of the model magnons. The spin chain of model 4 only has a dispersion along the chain axis, and the minimum energy is seen to be an average of the dispersive mode of model 2 for the interchain exchanges within the magnetic plane. Then these neutron spectroscopy models show $Ni(NCS)_2(pyzdo)_2$ to be well modeled by LSWT with model 2 to give $J_3 = J_y = 2.014$ meV, $J_5 = J_x = 0.235$ meV, and $D = -0.811$ meV, such that $\alpha = 0.12$. This neutron-spectroscopy-determined spatial anisotropy of exchange is like $\alpha = 0.17$ for the plane-wave DFT calculation.

H. Beyond LSWT

The neutron spectroscopy data were well reproduced by a LSWT model, but there is one pitfall with that analysis we consider. Moreover, there is the opportunity to compare the observed inelastic neutron scattering with a DMRG theory. Aside from the magnons, there are other observables available from a LSWT framework. Using the LSWT calculated ordered moment allows a cross-check of the model

FIG. 10. Neutron spectroscopy of $Ni(NCS)_2(pyzdo)_2$. These polycrystalline data are averaged from momentum transfers of 1 to 3 Å^{-1}. Models are as described in the text. The model 1 dashed red line is barely visible >5.7 meV, as it is nearly identical to models 2 and 4 in that region.

TABLE V. Neutron-scattering-derived spin-wave parameters for $Ni(NCS)_2(pyzdo)_2$. These values were used to generate the curves in Fig. 10 (negative D is easy-axis, and positive J is AFM).

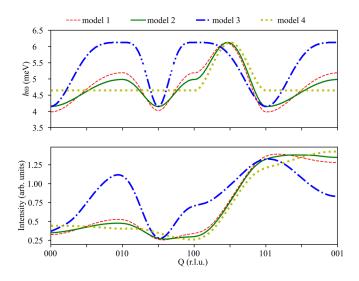|	Model 1	Model 2	Model 3	Model 4
J_1 (meV)	0.015	0	0	0
J_2 (meV)	−0.006	0	0	0
J_3 (meV)	1.964	2.014	1.125	1.992
J_4 (meV)	0.002	0	0	0
J_5 (meV)	0.340	0.235	1.125	0
D (meV)	−0.737	−0.811	−0.811	−1.068

FIG. 11. Comparison of linear spin-wave theory (LSWT) models for $Ni(NCS)_2(pyzdo)_2$. The momentum dependence of (a) energy transfer and (b) intensity are shown for the models described in the text.

with the measured magnetic neutron diffraction ordered moment. Thus, LSWT here refers to the Taylor expansion of the operator containing square roots in the Holstein-Primakoff (HP) transformation, keeping only the leading terms in the $1/S$ Taylor expansion that are bilinear in the HP boson ladder operators. As such, LSWT is only exact for certain cases, such as simple FMs at zero temperature and the limit of $S \to \infty$. Here, we consider two approximations beyond LSWT: (1) higher order in $1/S$ than LSWT and (2) DMRG theory of a spin chain in a static mean field that accounts for interchain interactions [32].

The magnon dispersion of a spatially anisotropic square lattice is

$$\hbar\omega = 2S(J_x + J_y + |D|)\sqrt{1 - \frac{[J_x \cos(q_x) + J_y \cos(q_y)]^2}{(J_x + J_y + |D|)^2}}.$$
(4)

Recalling that the HP transformation takes $S_z = S - a^\dagger a$ (the a operator annihilates an HP boson) [33], the first correction to the ordered moment (order $1/S^0$) may be written as

$$\Delta S = -\frac{1}{2} + \frac{1}{N}\sum_{\mathbf{q} \in \text{BZ}}\left(n_{\mathbf{q}} + \frac{1}{2}\right)\frac{1}{\sqrt{1 - \frac{[J_x \cos(q_x) + J_y \cos(q_y)]^2}{(J_x + J_y + |D|)^2}}},$$
(5)

where the summation of momentum ($\mathbf{q}$) is over the Brillouin zone (BZ), N is the number of momenta used, and $n_{\mathbf{q}}$ can be taken as a Bose population. Here, we consider the limit of temperature much less than the Hamiltonian parameter energies that are satisfied experimentally in the $T = 2$ K neutron spectroscopy data. The summation of Eq. (5) was found to converge when $\Delta q \leqslant 3 \times 10^{-3}$ r.l.u. The limiting case of $D \ll J_x$ or J_y reproduces the known result that $\Delta S = 0.197$ or for $S = 1$ that $\langle S_z \rangle = 0.803$ [34]. Conversely, as the anisotropy field (or a magnetic field) becomes much larger than J_x or J_y, $\Delta S \to 0$. Using the neutron-spectroscopy-derived parameters

TABLE VI. Hamiltonian parameters from fitting $Ni(NCS)_2(pyzdo)_2$ neutron spectra beyond LSWT.

	DMRG	RSWT model 4	DMRG	RSWT model 2
α	0	0	0.1	0.12
J_x (meV)	0	0	0.18	0.235
J_y (meV)	1.742	1.992	1.750	2.014
D (meV)	-3.011	-2.136	-2.415	-1.622
D/J_y	-1.729	-1.072	-1.380	-0.805
$\langle S_z \rangle$	0.947	0.929	0.933	0.924

of model 2, $\Delta S = 0.076$ and $\langle S_z \rangle = 0.924$ or $m_z = 1.848$ μ_B, which quantitatively reproduces the neutron diffraction value of $m_z = 1.8$ μ_B. Also, while an AFM spin chain without anisotropy does not support magnetic order even at zero temperature, the introduction of finite anisotropy quenches the fluctuations such that the neutron spectroscopy model 4 has $\Delta S = 0.071$.

Formally, there are an infinite number of terms to consider in the operator square root expansion, and the bookkeeping of these terms is nontrivial. The next order after LSWT contains four HP boson operator terms that include magnon-magnon interactions. For the Hartree-Fock-like decoupling of the next order diagrams of the magnon-magnon interactions, the expectation value of the number of HP bosons (i.e., ΔS) is an important quantity. We simply note that $\frac{\Delta S}{2S}$ is $\approx 4\%$ in the low-temperature limit for this material, so the real parameters of a renormalized spin-wave theory (RSWT) are to be similarly close to the reported LSWT parameters. Historically, there are many renormalized parameter spin-wave theories, of which Oguchi's work is an important early example [35].

Even in the absence of magnon-magnon interactions, LSWT single-ion anisotropy must be renormalized. This point may be illustrated by considering a system without exchange where the exact HP transformed Hamiltonian is

$$H = D\sum_i (S - a_i^\dagger a_i)^2 = D\sum_i S^2 - 2S a_i^\dagger a_i + a_i^\dagger a_i a_i^\dagger a_i.$$
(6)

The LSWT keeps only bilinear operators ($2S a_i^\dagger a_i$), snf the level spacing is $D2S$ and independent of the number of magnons. The exact solution has levels that are dependent on the number of magnons, and the spacing from the ground state to the first excited state is correctly $D(2S-1)$. In the low-temperature limit, a RSWT can be considered where the LSWT single-ion anisotropy is scaled by $(1 - \frac{1}{2S})$, Table VI. This rescaling of LSWT parameters is not specific to this system and should be included for any four HP term operators. A more detailed discussion of this anisotropy rescaling for SU(2) models in the context of classical magnetization theories can be found in Ref. [36].

The spin correlations of a spin chain in a static mean field may also be calculated with DMRG, and additional details are in the Appendix. The weaker J_x term is accounted as a staggered field, with $\alpha = 0.1$ from the LSWT best fit of the neutron spectroscopy and $\alpha = 0$ as for an isolated spin chain. Reproducing a single mode with no dispersion between chains as in the LSWT model 2, the DMRG Hamiltonian

parameters are shown in Table VI. While similar, the DMRG has lesser values for exchange and greater values for anisotropy than LSWT, with differences of 10% and more. The DMRG ordered moment of 0.933 is within a few percent of the spin-wave-adjusted [Eq. (5)] ordered moment.

I. Isothermal magnetization

The field dependence of magnetization gives further information about the Hamiltonian of the system. Here, experimental magnetization data are compared with calculated magnetizations for the best-fit results of the two frameworks for magnetic correlations: DMRG and LSWT. For LSWT, the calculation of the magnetic structure is done with the mean-field approximation, and LSWT is the next order correction in the $1/S$ expansion of the Hamiltonian. A mean-field model was generated using the anisotropy-renormalized best-fit parameters of model 2 in Table VI from the neutron spectroscopy along with the g factor from the magnetic susceptibility. The observation of finite single-ion anisotropy implies there is also g-factor anisotropy parallel and perpendicular to the unique axis as $D = \frac{\lambda}{2}(g_{||} - g_{\perp})$, where the free-ion spin-orbit parameter for Ni(II) is $\lambda = 906.4$ K $= 78.1$ meV [37]. In the coordination polymer, λ will be decreased compared with the free-ion value, so $g_{||} - g_{\perp} = 0.02$ is an upper limit, and these negligible effects will not be included in magnetization models here.

In the context of magnetization measurements, casting the interactions as field strengths provides some insight [38]. It is typical to consider an exchange field H_E and an anisotropy field H_A, and in definitions and comparisons, the explicit form of the Hamiltonian is important, as different conventions use different signs and different prefactors. Here, we use $H_E = \frac{4J_{2d}S}{g\mu_B}$ and $H_A = \frac{DS}{g\mu_B}$ to give the numerical values of $H_E = 37.2$ T and $H_A\mu_0 = -13.4$ T. Applying a field along the easy axis $\mathbf{B}||\mathbf{D}$, there will be a flop transition at H_E and saturation at $2H_E - H_A\mu_0 = 61.0$ T. Along the hard axis $\mathbf{B}\perp\mathbf{D}$, saturation occurs at $2H_E + H_A\mu_0 = 87.8$ T. Lower symmetry directions of the applied field require a model.

The mean-field model for Ni(NCS)$_2$(pyzdo)$_2$ uses the same Hamiltonian as Eq. (3) with the addition of Zeeman energy $(-g\mu_B \sum_i \mathbf{S}_i \cdot \mathbf{B})$. Expectation values of magnetization along the field direction were found by generating a two-spin $(S_1$ and $S_2)$ sublattice system and substituting expectation values $(\langle S_1 \rangle$ and $\langle S_2 \rangle)$ for the effect of the neighboring lattice due to superexchange using Hamiltonians H_1 and H_2 given by:

$$H_1 = DS_{1,z}^2 - g\mu_B\mathbf{S}_1 \cdot \mathbf{B} + 4J_{2d}\langle\mathbf{S}_2\rangle \cdot \mathbf{S}_1, \quad (7)$$

$$H_2 = DS_{2,z}^2 - g\mu_B\mathbf{S}_2 \cdot \mathbf{B} + 4J_{2d}\langle\mathbf{S}_1\rangle \cdot \mathbf{S}_2. \quad (8)$$

These four equations $(S_{1,x}, S_{1,z}, S_{2,x},$ and $S_{2,z})$ are self-consistently solved numerically using $S = 1$ quantum spins and statistical mechanics. Ten field-direction orientations in the x-z plane between $\mathbf{B}||\mathbf{D}$ and $\mathbf{B}\perp\mathbf{D}$ uniformly spaced in angle $(\hat{B} = [\sin\eta, \cos\eta])$ were calculated, Fig. 12. The spin-flop transition for $\mathbf{B}||\mathbf{D}$ is seen to round out and go to zero as the orientation approaches $\mathbf{B}\perp\mathbf{D}$. For the limit of $\mathbf{B}\perp\mathbf{D}$, there is no remnant of the spin flop, and the magnetizing process is simply a continuous rotation toward the field direction with increasing field until saturation.
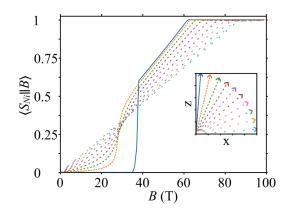

FIG. 12. Mean-field model of magnetization vs field for $T = 0.5$ K using neutron spectroscopy and magnetic susceptibility derived parameters for Ni(NCS)$_2$(pyzdo)$_2$. Ten different orientations of the applied field with respect to the anisotropy axis are shown. (inset) Directions of magnetic fields for magnetization calculations are shown. The anisotropy axis is along the z direction, and the dash spacings of the unit vectors correspond to the dash spacings of the lines for the expectation value of the magnetization along the field axis, $\langle S_{Ni} || \mathbf{B} \rangle$, shown in the main plot. The solid line is nearly $\mathbf{B}||\mathbf{D}$, while the dashed line with the largest spacing is nearly $\mathbf{B}\perp\mathbf{D}$.

The polycrystalline Ni(NCS)$_2$(pyzdo)$_2$ was measured in a pulsed field up to 90 T, with the measurement proportional to dM/dH and numerical integration performed to extract $M(H)$, Fig. 13. These data are compared with DMRG and a mean-field model with RSWT parameters of model 2, and semiquantitative agreement is found in both cases. Models and data show the characteristic S shape for a
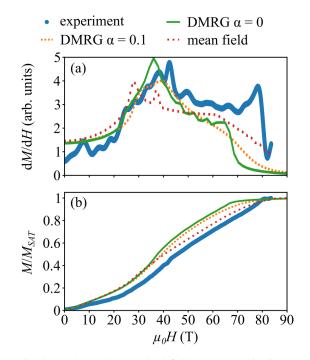

FIG. 13. Isothermal pulsed-field magnetization of Ni(NCS)$_2$(pyzdo)$_2$ at $T = 0.5$ K and models. Models are as described in the text. The (a) derivative of magnetization with respect to field and (b) the magnetization normalized to the saturation magnetization are shown.
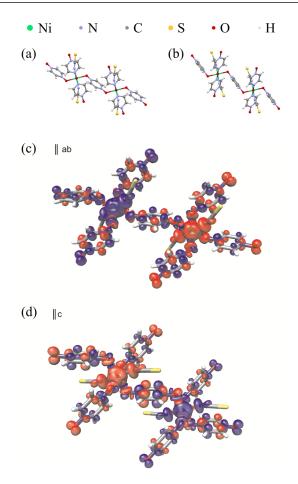
• Ni   • N   • C   • S   • O   · H

FIG. 14. Dimer models of $Ni(NCS)_2(pyzdo)_2$. (a) Along the J_5 $a, -b$ direction. (b) Along the J_3 c direction. (c) and (d) Views of the spin density distribution for the broken symmetry state of the dimer models. Isosurface value ± 0.001.

powder-averaged spin, with features lining up in field. Powder averaging the model is done by weighting each configuration to be $\propto \sin \eta$. Scaling of magnetization took the largest experimental value to be saturation, but the shape agreement illustrated by dM/dH shows better agreement at lower field with a different scaling.

J. Dimer-cluster DFT calculations

The exchange couplings along the bridging ligands were also investigated with a local basis-set DFT calculation. This local basis-set allows for a natural visualization and understanding of the magnetic orbitals in $Ni(NCS)_2(pyzdo)_2$ and provides an independent calculation (to compare with the experimental observations and the plane-wave DFT) of the spatial anisotropy of the superexchanges in the plane. This cluster approach approximates $Ni(NCS)_2(pyzdo)_2$ by the molecular building blocks for the superexchange constituents. Two nickel dimer clusters $[(pyzdo)_3Ni(NCS)_2(\mu\text{-}pyzdo)Ni(NCS)_2(pyzdo)_3]$ were considered to investigate J_3 (J_y) interactions along the c direction and J_5 (J_x) interactions along the $a, -b$ direction. Atomic positions were taken from the experimentally determined structure. These bond angle changes are accompanied by torsion angle differences of $47.55°$ ($a, -b$) vs $8.04°$ (c), which effectively decouples the pyzdo π system along $a, -b$, Figs. 14(a) and 14(b). The spin densities are larger for c-direction dimers (J_3) than $a, -b$ dimers (J_5), Figs. 14(c) and 14(d). Spin densities on the oxygen ions that bridge between nickel and pyzdo are 0.025 vs 0.044, for $a, -b$ and c directions, respectively. The superexchange energies for the dimers are listed in Table VII and are consistent with the plane-wave DFT and the neutron spectroscopy findings that the c-direction interactions are significantly stronger than the $a, -b$ direction. This calculation has $\alpha = 0.29$.

III. ADDITIONAL CONSIDERATIONS

In the preceding section, $Ni(NCS)_2(pyzdo)_2$ was shown to be well described as a spatially anisotropic $S = 1$ AFM with easy-axis single-ion anisotropy, spanning a variety of experimental and theoretical techniques. In this section, we report energies in meV (typical for neutron scattering) and report energies scaled by the Boltzmann constant to Kelvin (more common in some chemistry literature). Thus, the neutron spectroscopy parameters of the best fit are $J_x = 0.235$ meV (2.727 K), $J_y = 2.014$ meV (23.372 K), and an easy-axis single-ion anisotropy $D = -1.622$ meV (-18.823 K) after renormalization. The magnetic susceptibility data fit to the Lines model yielded a value for $J_{2d} = 1.15$ meV (13.35 K), which is strikingly like the J_{2d} value of 1.125 meV (13.06 K) from the neutron spectroscopy. The AFM ordering transition in zero magnetic field was similar in magnetic susceptibility (18 K), heat capacity (18.5 K), muon-spin relaxation (18.6 K), and neutron diffraction (17.5 K). The two different flavors of DFT calculations, cluster and plane-wave, were able to predict the spatial anisotropy of the magnetic interactions. Both cluster and plane-wave DFT, as parameterized here, predict the correct order of magnitude for the magnetic interactions. While the DFT parameters could in principle be further refined against the neutron spectroscopy values for the magnetic interactions, this is beyond the scope of this paper, the main point of which is to demonstrate the relative magnitudes of the exchanges that show a high degree of spatial anisotropy. The neutron spectroscopy experimentally shows the requirement of spatial anisotropy to reproduce the observed spin-spin correlations. While five interactions were used in the plane-wave DFT model, only the dominant two were included in the neutron spectroscopy fits, as the polycrystalline data contain insufficient features to constrain a more detailed model.

TABLE VII. Model superexchange values and definitions from DFT for $Ni(NCS)_2(pyzdo)_2$.

Index	Distance (Å)	Direction vector	Lattice direction	Orientation from magnetic structure	J_{ORCA} (meV)
J_3	8.08	0,0,1	C	AFM	3.66
J_5	8.38	1,−1,0	$a, -b$	AFM	1.07

mean field: simulation (-●-), fit (—)
classical (α=0): simulation (-★-), fit (·····)
classical (α=0.12): simulation (-■-), fit (-··-)
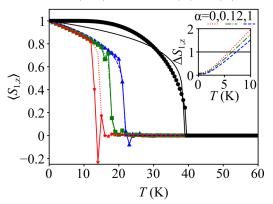classical (α=1): simulation (-▲-), fit (---)

FIG. 15. Comparison of different models for the $Ni(NCS)_2(pyzdo)_2$ thermal phase transition, details described in the text. (inset) Temperature dependence of the linear spin-wave theory (LSWT) correction to the ordered moment.

TABLE VIII. Fits of Fig. 15 data to $\langle S_{1,Z}(T) \rangle = [1 - (\frac{T}{T_N})]^{\beta}$.

	T_N	β
Classical ($\alpha = 0$)	15.0	0.13
Classical ($\alpha = 0.12$)	18.0	0.16
Classical ($\alpha = 1$)	21.6	0.19
Mean-field	38.5	0.18

If sufficiently large single crystals of $Ni(NCS)_2(pyzdo)_2$ are made, the additional neutron spectroscopy of a single crystal (or oriented array) will allow for a more detailed model refinement. The isothermal magnetization deep within the ordered state was modeled with a high degree of accuracy using neutron-spectroscopy-derived parameters, whether with RSWT connected to mean-field theory or with DMRG, although there are subtle disagreements between the models and the data. The origin of the difference between DMRG and RSWT parameters is not totally clear and merits further investigation. For one-dimensional (1D) problems, DMRG has been shown to excellently reproduce experimental observations, and LSWT is expected to perform well for magnetic systems deep in the ordered state with a small number of magnons. For this $Ni(NCS)_2(pyzdo)_2$ system that is quasi-1D, both RSWT (plus mean-field theory) and DMRG provide valuable information about the ground state, and it is not clear which is entirely better for the magnetic-field-dependent low-temperature data, but the neutron spectroscopy data are better reproduced by the 2D model (not DMRG).

Here, we further consider the thermal phase transition in zero magnetic field. While mean-field theory of magnetization performs well for highly three-dimensional magnetically ordered systems in the low-temperature limit, it fails at finite temperatures and lower dimensions. Using the neutron-spectroscopy-derived parameters with a renormalized D, mean-field theory yields a phase transition in the sublattice magnetization at $T_N = 40$ K, Fig. 15, overestimating the $T_N = 18.5$ K from heat capacity data by a factor of 2.2. Note that, in mean-field theory, the sublattice magnetization saturates to the full spin value. In the low-temperature limit, quantum and thermal fluctuations can be included with LSWT by using the Bose factor for the magnon number, reproducing well the observed ordered moment at low temperature and zero magnetic field, but a quantitative prediction of the ordered temperature cannot be made, only that 1D models fluctuate more than 2D (Fig. 15 inset) and the LSWT Taylor expansion of the

operator square roots is violated before the system achieves the experimentally determined region of criticality. Due to the abundant experimental characterization of $Ni(NCS)_2(pyzdo)_2$ here, it is edifying to consider a classical spin-dynamics approach [39–41] of the thermal phase transition. Using the same parameters as for the mean-field temperature scan, three simulations were performed with $\alpha = 0$ (spin chain), $\alpha = 0.12$ (spatially anisotropic square lattice), and $\alpha = 1$ (spatially isotropic square lattice), and details are in the Appendix. The temperature dependences of the sublattice magnetizations are shown in Fig. 15. These classical simulations can account for the spatial anisotropy of the interactions, and the quantitative agreement of the $\alpha = 0.12$ result (Table VIII) to the experimental results suggests this approximation to extract T_C will be of good quality for similar systems. The classical simulations all saturate to the full $S = 1$ magnetization at low temperature, not capturing the quantum fluctuations. Insofar as the neutron-spectroscopy-derived parameters quantitatively reproduce the observed magnetic ordering temperature in the classical simulation, these data also illustrate the relative smallness of any interplane interactions and support the 2D magnetism model of $Ni(NCS)_2(pyzdo)_2$.

It is informative to consider the phase diagram in magnetic field and temperature of $Ni(NCS)_2(pyzdo)_2$ as a spatial anisotropy square-lattice AFM with single-ion anisotropy. In Fig. 16, the mean-field results for $\mathbf{B} \perp \mathbf{D}$ and $\mathbf{B} \parallel \mathbf{D}$ are shown, with a temperature axis that was scaled linearly to overlay the experimental and mean-field T_N. For $\mathbf{B} \perp \mathbf{D}$, there is an arc that connects the zero-temperature saturation critical field to the zero-field critical temperature. For $\mathbf{B} \parallel \mathbf{D}$, there are two lines: the saturation field and the flop field. Plotting the heat capacity data points from Fig. 3 for the polycrystalline sample, the trend of the phase line is reproduced, but there is a quantitative disagreement with the scaled mean-field critical line. There is scatter between the DMRG and mean-field models as compared with the experimental low-temperature (polycrystalline) saturating field. For the isothermal magnetization, transitions were estimated from visual inflections in the data. First, there is the steep rise seen ∼24 T, then the field at which the gradient begins to decrease ∼ 41 T, and finally the kink at 80 T. Any further analysis of data in a magnetic field really needs single-crystalline samples.

IV. SUMMARY AND CONCLUSIONS

In summary, we have thoroughly characterized the magnetic Hamiltonian of the $Ni(NCS)_2(pyzdo)_2$ coordination polymer, which is found by x-ray diffraction to consist of Ni-pyzdo layers held apart by N-O···H hydrogen bonds. The magnetometry, heat capacity, and muon-spin relaxation data clearly show that the material orders AFM < 18.5 K.

····· mean field $B \perp D$
--- mean field $B \| D$, flop
-·- mean field $B \| D$, sat

★ experiment, Cp
● experiment, dM/dH

DMRG $B \perp D$: α=0(···), α=0.1(···)
DMRG $B \| D$, flop : α=0(▲--), α=0.1(■--)
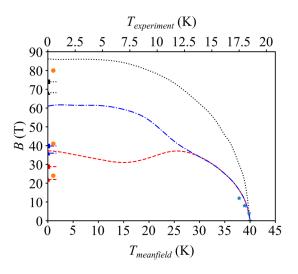DMRG $B \| D$, sat : α=0(▲·-), α=0.1(■·-)

FIG. 16. $Ni(NCS)_2(pyzdo)_2$ phase diagram.

Analysis of elastic and inelastic neutron scattering results provide estimates for the in-plane exchange and anisotropy energies and confirms that the material is a highly anisotropic square-lattice AFM with easy-axis single-ion anisotropy, in keeping with the DFT predictions. We also discuss the results of DMRG theory considering the experimental findings. The detection of a collinearly ordered magnet ground state is in line with the phase diagram of anisotropy and interchain interactions for a quasi-1D system [19]. From a materials discovery standpoint, the pyrazine dioxide ligand (pyzdo) shows a markedly greater superexchange than the pyrazine ligand [5], lighting a pathway for further engineered magnetic interactions in these coordination polymers. Mean-field theory using parameters from neutron spectroscopy modeling with RSWT semiquantitatively reproduces the measured magnetization, as do DMRG parameters derived from neutron spectroscopy. Looking forward to possible extensions of this work, synthesis of large single crystals or a ligand modification to reduce the saturation field will provide additional information on the present system. In addition, the chosen combination of magnetic and structural probes has been shown here to provide a complete description of the magnetism in this class of highly tunable molecular system at the level of a low-energy Hamiltonian. This same approach will prove useful in the characterization of similar magnetic systems in terms of low-dimensional magnetic models.

ACKNOWLEDGMENTS

APPENDIX: EXPERIMENTAL AND NUMERICAL DETAILS

1. Synthesis

In a typical synthesis, 0.2709 g of $Ni(NO_3)_2.6H_2O$ (0.93 mmol) and 0.1489 g (1.96 mmol) of NH_4NCS were dissolved separately in 10 mL of H_2O and then slowly mixed. To this solution was added 0.2089 g (1.86 mmol) of pyrazine-n, n'-dioxide to give a green colored solution. The solution was covered with parafilm and perforated with a few holes to allow slow solvent evaporation. Upon standing at room temperature for $\sim$ 1 week, brown colored crystals formed in the flask. After the second week, more crystals emerged from solution, and the combined mass was collected by suction filtration, washed with 2×5 mL aliquots of fresh H_2O and dried *in vacuo*. The yield, though not optimized, was 76% (0.2820 g). A scaled-up synthesis was carried out to produce the neutron sample; 3.0907 g of brown crystals were obtained (86% yield).

2. X-ray diffraction

A crystal of $Ni(NCS)_2(pyzdo)_2$ was removed from the flask, a suitable crystal was selected, attached to a glass fiber, and data were collected at 90(2) K using a Bruker/Siemens SMART APEX instrument (Mo $K\alpha$ radiation, $\lambda = 0.71073$ Å) equipped with a Cryocool NeverIce

TABLE IX. Crystal data and structure refinement for Ni(NCS)$_2$(pyzdo)$_2$.

Empirical formula	C$_{10}$ H$_8$ N$_6$ Ni O$_4$ S$_2$
Formula weight	399.05
Temperature	90(2) K
Wavelength	0.71073 Å
Crystal system	Triclinic
Space group	*P*-1
Unit cell dimensions	$a = 6.8727(4)$ Å $a = 82.7230(13)°$.
	$b = 7.0431(4)$ Å $b = 66.8030(12)°$.
	$c = 8.0772(4)$ Å $g = 74.0820(13)°$.
Volume	345.51(3) Å^3
Z	1
Density (calculated)	1.918 Mg/m^3
Absorption coefficient	1.737 mm^{-1}
F(000)	202
Crystal size	0.25×0.20×0.04 mm^3
Crystal color and habit	Orange plate
Diffractometer	Bruker/Siemens SMART APEX
θ range for data collection	2.74–25.25°
Index ranges	$-7 \leqslant h \leqslant 8, \; -8 \leqslant k \leqslant 8, \; 0 \leqslant l \leqslant 9$
Reflections collected	9020
Independent reflections	1251 [$R_{\rm int} = 0.0000$]
Completeness to $\theta = 25.25°$	100.0%
Absorption correction	Semiempirical from equivalents
Max and min transmission	0.9338 and 0.6706
Solution method	Bruker, 2003; XS, SHELXTL v. 6.14
Refinement method	Full-matrix least-squares on F^2
Data/restraints/parameters	1251/0/107
Goodness-of-fit on F^2	1.088
Final *R* indices [$I > 2\sigma(I)$]	R1 = 0.0227, wR2 = 0.0621
R indices (all data)	R1 = 0.0242, wR2 = 0.0629
Largest diff. peak and hole	0.367 and -0.271 e Å^{-3}

low-temperature device. Data were measured using ω scans of 0.3° per frame for 10 s, and a partial sphere of data was collected. A total of 2100 frames were collected with a final resolution of 0.83 Å. Cell parameters were retrieved using SMART [43] software. The data were rotationally twinned and were deconvoluted using CELL_NOW [44] giving a two-component twin relationship: 179.8° rotation about the reciprocal axis 1.000, 0.000, 0.002, with a refined twinning ratio of 0.277(5). The matrix used to relate the second orientation to the first domain is

$$\begin{bmatrix} -0.765 & -0.231 & -0.236 \\ -0.824 & -0.184 & 0.816 \\ -0.953 & 0.950 & -0.051 \end{bmatrix}.$$

Each cell component was refined using SAINTPLUS [45] on all observed reflections. Data reduction and correction for Lp and decay were performed using SAINTPLUS software. Absorption corrections were applied using TWINABS [46]. The structure was solved by direct methods and refined by least squares method on F^2 using the SHELXTL program package [47]. The structure was solved in the space group *P*-1 (#2) by analysis of systematic absences. All nonhydrogen atoms were refined anisotropically. No decomposition was observed during data collection. Details of the data collection and refinement are given in Table IX. Atomic coordinates, select bond lengths and angles, and anisotropic displace parameters

are given in Tables X–XII, respectively. Further details are provided in the Supplemental Material [28].

3. Magnetic susceptibility

Magnetic susceptibility was performed with a vibrating sample magnetometer.

TABLE X. Atomic coordinates ($\times 10^4$) and equivalent isotropic displacement parameters (Å$^2 \times 10^3$) for Ni(NCS)$_2$(pyzdo)$_2$. U(eq) is defined as one third of the trace of the orthogonalized U^{ij} tensor.

	x	y	z	U(eq)
C(3)	6830(3)	4093(3)	336(3)	13(1)
C(4)	3027(3)	4978(3)	1295(2)	12(1)
C(7)	8415(3)	445(3)	4297(2)	13(1)
C(8)	10739(3)	1471(3)	5302(2)	13(1)
C(10)	6580(3)	7967(3)	1831(3)	12(1)
N(2)	4851(3)	4095(2)	1626(2)	11(1)
N(6)	9156(3)	1917(2)	4600(2)	12(1)
N(9)	5718(3)	7133(2)	3144(2)	14(1)
Ni(1)	5000	5000	5000	11(1)
O(1)	4706(2)	3262(2)	3221(2)	13(1)
O(5)	8383(2)	3777(2)	4207(2)	15(1)
S(1)	7835(1)	9106(1)	$-5(1)$	17(1)

TABLE XI. Bond lengths (Å) and angles (deg) for $Ni(NCS)_2(pyzdo)_2$.

C(3)-N(2)	1.349(2)
C(3)-C(4)#1[a]	1.374(3)
C(3)-H(3)	0.9500
C(4)-N(2)	1.351(3)
C(4)-C(3)#1[a]	1.374(3)
C(4)-H(4)	0.9500
C(7)-N(6)	1.359(2)
C(7)-C(8)#2[a]	1.368(3)
C(7)-H(7)	0.9500
C(8)-N(6)	1.362(3)
C(8)-C(7)#2[a]	1.368(3)
C(8)-H(8)	0.9500
C(10)-N(9)	1.166(3)
C(10)-S(1)	1.630(2)
N(2)-O(1)	1.3246(19)
N(6)-O(5)	1.321(2)
N(9)-Ni(1)	2.0004(16)
Ni(1)-N(9)#3[a]	2.0004(16)
Ni(1)-O(1)	2.1006(12)
Ni(1)-O(1)#3[a]	2.1006(12)
Ni(1)-O(5)	2.1038(13)
Ni(1)-O(5)#3[a]	2.1038(13)
N(2)-C(3)-C(4)#1[a]	119.65(18)
N(2)-C(3)-H(3)	120.2
C(4)#1-C(3)-H(3)[a]	120.2
N(2)-C(4)-C(3)#1[a]	120.50(18)
N(2)-C(4)-H(4)	119.7
C(3)#1-C(4)-H(4)[a]	119.7
N(6)-C(7)-C(8)#2[a]	119.87(18)
N(6)-C(7)-H(7)	120.1
C(8)#2-C(7)-H(7)[a]	120.1
N(6)-C(8)-C(7)#2[a]	120.50(17)
N(6)-C(8)-H(8)	119.8
C(7)#2-C(8)-H(8)[a]	119.8
N(9)-C(10)-S(1)	178.79(19)
O(1)-N(2)-C(3)	119.80(16)
O(1)-N(2)-C(4)	120.36(15)
C(3)-N(2)-C(4)	119.84(16)
O(5)-N(6)-C(7)	121.07(16)
O(5)-N(6)-C(8)	119.30(15)
C(7)-N(6)-C(8)	119.63(16)
C(10)-N(9)-Ni(1)	162.12(15)
N(9)#3-Ni(1)-N(9)[a]	180.000(1)
N(9)#3-Ni(1)-O(1)[a]	86.81(6)
N(9)-Ni(1)-O(1)	93.19(6)
N(9)#3-Ni(1)-O(1)#3[a]	93.19(6)
N(9)-Ni(1)-O(1)#3[a]	86.81(6)
O(1)-Ni(1)-O(1)#3[a]	180.00(4)
N(9)#3-Ni(1)-O(5)[a]	92.71(6)
N(9)-Ni(1)-O(5)	87.29(6)
O(1)-Ni(1)-O(5)	93.08(5)
O(1)#3-Ni(1)-O(5)[a]	86.92(5)
N(9)#3-Ni(1)-O(5)#3[a]	87.29(6)
N(9)-Ni(1)-O(5)#3[a]	92.71(6)
O(1)-Ni(1)-O(5)#3[a]	86.92(5)
O(1)#3-Ni(1)-O(5)#3[a]	93.08(5)

TABLE XI. (*Continued.*)

O(5)-Ni(1)-O(5)#3[a]	180.0
N(2)-O(1)-Ni(1)	115.25(10)
N(6)-O(5)-Ni(1)	120.93(11)

[a]Symmetry transformations used to generate equivalent atoms: #1 : $-x + 1, -y + 1, -z$; #2 : $-x + 2, -y, -z + 1$; and #3 : $-x + 1, -y + 1, -z + 1$.

4. Heat capacity

Heat capacity (C_p) measurements were carried out using a 14 T Quantum Design PPMS, with a 2.1 mg polycrystalline sample secured to an alumina stage sample platform using a thin layer of Apiezon-N grease to ensure good thermal contact. This platform also houses a Cernox thermometer and an electric heater that is connected to the temperature bath using gold wires. The sample was cooled in zero magnetic field under high vacuum to the base temperature of 1.8 K and the data collected upon heating up to 100 K. More scans were taken between 1.8 and 25 K at zero field as well as 4, 8, and 12 T. The C_p was measured using a standard thermal relaxation technique [48]. For this technique, a heat pulse ($\approx 2\%$ of the thermal bath temperature) was applied to the stage and C_p evaluated by measuring the time constant of the thermal decay curve. The heat capacities of the Apiezon-N grease and sample platform were measured separately and subtracted from the total to obtain the heat capacity of the sample.

5. Muon-spin relaxation

Zero-field muon-spin relaxation (μ^+SR) measurements were performed on $Ni(NCS)_2(pyzdo)_2$ using the GPS spectrometer at the Swiss Muon Source, Paul Scherrer Institut, Villigen, Switzerland. For the measurement, the sample was packed in an Ag foil packet and suspended in the muon beam inside a ^{4}He cryostat. In the measurement, spin-polarized positive muons are implanted into the sample. The positive muons stop in the material, usually in sites with high electron density, and their polarized magnetic moments

TABLE XII. Anisotropic displacement parameters ($\mathrm{Å}^2 \times 10^3$) for $Ni(NCS)_2(pyzdo)_2$. The anisotropic displacement factor exponent takes the form: $-2\pi^2(h^2a^{*2}U^{11} + \cdots + 2hka^*b^*U^{12})$.

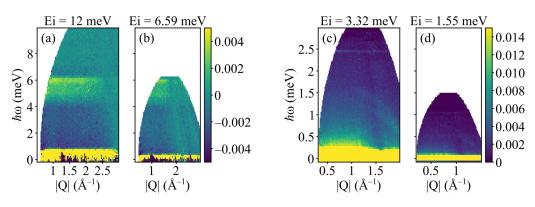|	U^{11}	U^{22}	U^{33}	U^{23}	U^{13}	U^{12}
C(3)	13(1)	11(1)	15(1)	−3(1)	−6(1)	−2(1)
C(4)	12(1)	11(1)	13(1)	−3(1)	−4(1)	−2(1)
C(7)	12(1)	15(1)	12(1)	−1(1)	−5(1)	−3(1)
C(8)	12(1)	15(1)	12(1)	−2(1)	−4(1)	−4(1)
C(10)	12(1)	11(1)	17(1)	−5(1)	−8(1)	0(1)
N(2)	16(1)	9(1)	11(1)	−1(1)	−6(1)	−4(1)
N(6)	11(1)	11(1)	11(1)	0(1)	−2(1)	−1(1)
N(9)	16(1)	12(1)	13(1)	0(1)	−6(1)	−3(1)
Ni(1)	12(1)	10(1)	10(1)	1(1)	−5(1)	−3(1)
O(1)	19(1)	12(1)	8(1)	2(1)	−7(1)	−5(1)
O(5)	14(1)	9(1)	19(1)	3(1)	−7(1)	−1(1)
S(1)	17(1)	16(1)	17(1)	3(1)	−3(1)	−6(1)

FIG. 17. Intensity maps of $Ni(NCS)_2(pyzdo)_2$ experimental neutron spectroscopy data. (a) $Ei = 12$ meV, $T = 2$ K $- T = 22$ K data. (b) $Ei = 6.59$ meV, $T = 2$ K $- T = 22$ K data. (c) $Ei = 3.32$ meV, $T = 2$ K data. (d) $Ei = 1.55$ meV, $T = 2$ K data. White regions are where the scattering condition is not satisfied by the spectrometer.

precess around the direction of the local magnetic field with frequency $\nu = \gamma_\mu B/2\pi$, where the muon gyromagnetic ratio $2\pi \times 135.5$ MHzT^{-1}. Muons are unstable with mean lifetime 2.2 μs and decay into a positron and two neutrinos, the former being preferentially emitted along the direction of muon spin. Detectors record the direction of positron emission, whose time dependence tracks the average spin polarization of the muon ensemble. The detectors are divided into forward (F) and backward (B) detector banks, and the direction of preferential positron emission is represented by the asymmetry between $N_F(t)$ and $N_B(t)$, the number of positrons detected in each detector bank as a function of time. The asymmetry function, which is proportional to the average spin polarization of the muon ensemble, is defined as $A(t) = \frac{N_F(t) - \epsilon N_B(t)}{N_F(t) + \epsilon N_B(t)}$, where ϵ is an experimentally determined parameter dependent on apparatus geometry and detector efficiency [30,49].

6. Neutron diffraction

Neutron diffraction was performed at the time-of-flight Wish diffractometer of the ISIS Neutron Source [50]. Rietveld refinements were performed using the FULLPROF program [51].

7. Plane-wave DFT

For plane-wave DFT, VASP software [52,53] was used with the generalized gradient approximation functional of Perdew-Burke-Ernzerhof as PBE [54]. The projector augmented-wave method [55,56] was used for valence electrons with the included pseudopotentials applied via the PBE.54 files. The on-site Coulomb interaction was included with the rotationally invariant approach having $U_{Ni} = 5$ eV and $J_{Ni} = 1$ eV. A Γ-centered mesh was generated with $(4 \times 2 \times 4)$ k-points, and plane waves were cut above a kinetic energy of 500 eV.

8. Neutron spectroscopy

Inelastic neutron scattering of polycrystalline $Ni(NCS)_2(pyzdo)_2$ was performed on the cold chopper neutron spectrometer [57,58] using the high-flux mode at the Spallation Neutron Source of Oak Ridge National Laboratory.

Models were fit to integrations over momentum described in the main text, as no clear momentum-dependent features were seen, Fig. 17. No magnetic inelastic scattering was observed $< \approx 4$ meV.

9. LSWT for neutron spectroscopy

The LSWT SpinWaveGenie library was used to generate neutron scattering intensities from spin models [59]. Powder averages in momentum were done by taking a set of momentum from 1 to 3 Å^{-1} with 0.1 Å^{-1} steps and for each momentum sampling all orientations equally by approximating the surface tiling of a sphere with a golden spiral. The energy resolution of the spectrometer was used in generating model spectra.

10. DMRG theory

Calculations were performed for $D/J_y = [-0.5, -1.0, -1.5]$ using $L = 64$ sites on a 1D system with open boundary conditions. The effect of coupling to $z_\perp = 2$ nearest-neighbor chains is treated within self-consistent mean-field approximation [32,60] with interchain coupling $\alpha = J_x/J_y = z_\perp J_5/J_3$ of model 2 in Table V (here, we have used the notation as in Ref. [61]). The latter results in $m_z = [0.851, 0.909, 0.938]$ staggered magnetic moment, for $D/J_y = [-0.5, -1.0, -1.5]$, respectively. Throughout the DMRG [62–65] procedure, up to $M \approx 2048$ states are kept and ≈ 15 full sweeps are performed in the finite-sized algorithm, maintaining the truncation error $< 10^{-6}$. We have chosen $\delta\omega/J_y = 0.04$ as the frequency resolution [66] with broadening $\eta = 2\omega$.

The spin-spin correlation functions from DMRG are dominated by a single mode in the $\langle S_+ S_- \rangle$ channel, Fig. 18. The effect of changing D/J_y and the mean-field interactions is illustrated by the change in the energy of the mode position at the BZ center and edge, Fig. 19. The D/J_y dependences of the mode parameters were fit with a quadratic equation to interpolate and extract parameters from the experimental data. The result of this extraction is in Table VI. These DMRG spectra are well parameterized by fitting to an effective LSWT, also in Fig. 18, which capture the dominant mode.
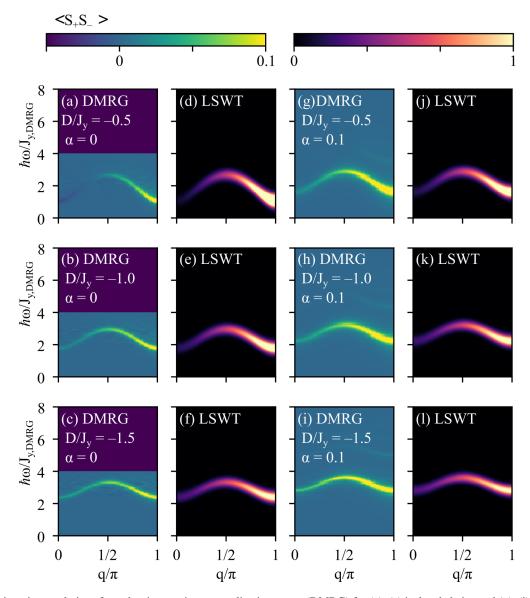
FIG. 18. Spin-spin correlations from density matrix renormalization group (DMRG) for (a)–(c) isolated chains and (g)–(i) chains interacting via a mean-field as described in the text. For (a)–(c), the region $> 4J$ was not calculated. Fits of the DMRG to linear spin-wave theory (LSWT) are shown to the right of the respective spectra, with the LSWT parameters plotted in Fig. 20.

The dominant transverse mode of DMRG was fit using LSWT to compare the parameters from each model,
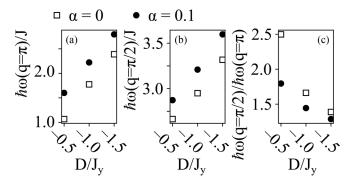

FIG. 19. Comparison of the dominant transverse density matrix renormalization group (DMRG) mode at (a) the Brillouin zone (BZ) center, (b) the BZ edge, and (c) their ratio as a function of D/J_y.

Fig. 20. All three $D_{DMRG}/J_{y,DMRG}$ ratios are in a long-range magnetically ordered ground state. The effect of numerical values for single-ion anisotropy and exchange are consistently different between DMRG and RSWT. The RSWT parameters may be extracted by scaling these LSWT anisotropy values by a factor of 2.

11. Pulse-field magnetization

Experimental data from the 60 and 100 T magnets were stitched together at 45 T. Pulsed-field measurements were made up to 60 T using a 1.5 mm bore, 1.5 mm long, 1500 turn compensated-coil susceptometer constructed from a 50 gauge high-purity copper wire. When the sample is within the coil, the signal voltage V is proportional to dM/dt, where t is time. Numerical integration of V is used to evaluate M. The sample is mounted within a 1.3-mm-diameter ampoule that can be moved in and out of the coil [67]. Accurate values of
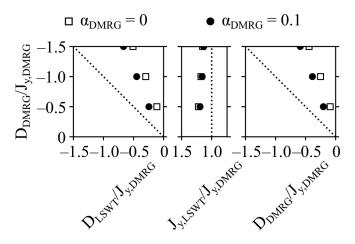
FIG. 20. Comparison of density matrix renormalization group (DMRG) and linear spin-wave theory (LSWT) parameterizations of a spin-chain mode.

M were obtained by subtracting empty-coil data from those measured under identical conditions with the sample present. The susceptometer was placed inside a ^{3}He cryostat providing a base temperature of 0.5 K. The magnetic field was measured by integrating V induced in a 10 turn coil calibrated by observing the de Haas–van Alphen oscillations of the belly orbits of the copper wires in the susceptometer coil [68]. The dM/dH were generated by a numerical derivative followed by a 1 T FWHM Gaussian smoothing.

12. Local basis-set DFT

For evaluation of the exchange couplings along the bridging pyzdo ligands, the broken-symmetry (BS) approach of Noodleman [69] as implemented in the ORCA ver. 4.2 suite of programs [70–72] was employed. The formalism of Yamaguchi *et al.* [73], which employs calculated expectation values $\langle S^2 \rangle$ for both high-spin and BS states was used [74]. Calculations related to magnetic interactions have been performed using the PBE0 functional. The Ahlrichs-VTZ basis function set was used [75]. Spin densities were visualized using the UCSF Chimera program ver. 1.8.

13. Classical magnetization model

These simulations used the Langevin method of the Sunny.jl package [41]. The input parameters of nsamples = 1×10^6, $\lambda = 0.1$, thermdur = 10, decorrdur = 0.5, and $\Delta t = 5 \times 10^{-3}$ were used. Periodic boundary conditions and 64 sites were used, with 8×8 for the 2D models and 1×64 for the spin chain.

[1] A. Vasiliev, O. Volkova, E. Zvereva, and M. Markina, npj Quantum Mater. **3**, 18 (2018).

[2] B. M. Huddart, J. Brambleby, T. Lancaster, P. A. Goddard, F. Xiao, S. J. Blundell, F. L. Pratt, J. Singleton, P. MacChi, R. Scatena *et al.*, Phys. Chem. Chem. Phys. **21**, 1014 (2019).

[3] J. L. Manson, Q. Z. Huang, C. M. Brown, J. W. Lynn, M. B. Stone, J. Singleton, and F. Xiao, Inorg. Chem. **54**, 11897 (2015).

[4] B. Gillon, A. Hammerschmied, A. Gukasov, A. Cousson, T. Cauchy, E. Ruiz, J. A. Schlueter, and J. L. Manson, Eur. J. Inorg. Chem. **2018**, 278 (2018).

[5] J. Liu, P. A. Goddard, J. Singleton, J. Brambleby, F. Foronda, J. S. Möller, Y. Kohama, S. Ghannadzadeh, A. Ardavan, S. J. Blundell *et al.*, Inorg. Chem. **55**, 3515 (2016).

[6] P. A. Goddard, J. Singleton, I. Franke, J. S. Möller, T. Lancaster, A. J. Steele, C. V. Topping, S. J. Blundell, F. L. Pratt, C. Baines *et al.*, Phys. Rev. B **93**, 094430 (2016).

[7] W. J. A. Blackmore, J. Brambleby, T. Lancaster, S. J. Clark, R. D. Johnson, J. Singleton, A. Ozarowski, J. A. Schlueter, Y. S. Chen, A. M. Arif *et al.*, New J. Phys. **21**, 093025 (2019).

[8] J. L. Manson, Z. E. Manson, A. Sargent, D. Y. Villa, N. L. Etten, W. J. A. Blackmore, S. P. M. Curley, R. C. Williams, J. Brambleby, P. A. Goddard *et al.*, Polyhedron **180**, 114379 (2020).

[9] W. J. A. Blackmore, S. P. M. Curley, R. C. Williams, S. Vaidya, J. Singleton, S. Birnbaum, A. Ozarowski, J. A. Schlueter, Y. S. Chen, B. Gillon *et al.*, Inorg. Chem. **61**, 141 (2022).

[10] D. M. Pajerowski, A. P. Podlesnyak, J. Herbrych, and J. Manson, Phys. Rev. B **105**, 134420 (2022).

[11] E. Mun, F. Weickert, J. Kim, B. L. Scott, C. F. Miclea, R. Movshovich, J. Wilcox, J. Manson, and V. S. Zapf, Phys. Rev. B **93**, 104407 (2016).

[12] X. G. Wen, Rev. Mod. Phys. **89**, 041004 (2017).

[13] H. C. Jiang, F. Krüger, J. E. Moore, D. N. Sheng, J. Zaanen, and Z. Y. Weng, Phys. Rev. B **79**, 174409 (2009).

[14] A. S. Moskvin, J. Exp. Theor. Phys. **121**, 477 (2015).

[15] X. Bai, S. S. Zhang, Z. Dun, H. Zhang, Q. Huang, H. Zhou, M. B. Stone, A. I. Kolesnikov, F. Ye, C. D. Batista *et al.*, Nat. Phys. **17**, 467 (2021).

[16] F. D. M. Haldane, Phys. Rev. Lett. **50**, 1153 (1983).

[17] F. D. M. Haldane, Phys. Lett. A **93**, 464 (1983).

[18] F. D. M. Haldane, Rev. Mod. Phys. **89**, 040502 (2017).

[19] T. Sakai and M. Takahashi, Phys. Rev. B **42**, 4537 (1990).

[20] Y. J. Kim and R. J. Birgeneau, Phys. Rev. B **62**, 6378 (2000).

[21] R. Zinke, J. Schulenburg, and J. Richter, Eur. Phys. J. B **61**, 147 (2008).

[22] A. Prescimone, C. Morien, D. Allan, J. A. Schlueter, S. W. Tozer, J. L. Manson, S. Parsons, E. K. Brechin, and S. Hill, Angew. Chem. **124**, 7608 (2012).

[23] J. A. Schlueter, H. Park, G. J. Halder, W. R. Armand, C. Dunmars, K. W. Chapman, J. L. Manson, J. Singleton, R. McDonald, A. Plonczak *et al.*, Inorg. Chem. **51**, 2121 (2012).

[24] H. L. Sun, S. Gao, B. Q. Ma, and G. Su, Inorg. Chem. **42**, 5399 (2003).

[25] H. L. Sun, B. Q. Ma, S. Gao, and G. Su, Chem. Commun. **1**, 2586 (2001).

[26] M. James, Aust. J. Chem. **55**, 219 (2002).

[27] X. Zhao, Z. Y. Zhao, L. M. Chen, X. Rao, H. L. Che, L. G. Chu, H. D. Zhou, L. S. Ling, J. F. Wang, and X. F. Sun, Phys. Rev. B **99**, 104419 (2019).

[28] See Supplemental Material at http://link.aps.org/supplemental/10.1103/PhysRevB.108.094425 for x-ray CIF, neutron CIF, and neutron mCIF.

[29] M. E. Lines, J. Phys. Chem. Solids **31**, 101 (1970).

[30] S. J. Blundell, S. Blundell, R. De Renzi, T. Lancaster, and F. L. Pratt, *Muon Spectroscopy: An Introduction* (Oxford University Press, Oxford, 2022).

[31] L. Onsager, Phys. Rev. **65**, 117 (1943).

[32] H. J. Schulz, Phys. Rev. Lett. **77**, 2790 (1996).

[33] R. S. Fishman, J. A. Fernandez-Baca, and T. Rõõm, *Spin-Wave Theory and Its Applications to Neutron Scattering and THz Spectroscopy* (Morgan and Claypool, San Rafael, 2018).

[34] D. A. Huse, Phys. Rev. B **37**, 2380 (1988).

[35] T. Oguchi, Phys. Rev. **117**, 117 (1960).

[36] D. Dahlbom, H. Zhang, Z. Laraib, D. M. Pajerowski, K. Barros, and C. Batista, arXiv:2304.03874.

[37] B. N. Figgis and M. A. Hitchman, *Ligand Field Theory and Its Applications* (Wiley-VCH, New York, 2000).

[38] L. J. De Jongh and A. R. Miedema, Adv. Phys. **23**, 1 (1974).

[39] D. Dahlbom, H. Zhang, C. Miles, X. Bai, C. D. Batista, and K. Barros, Phys. Rev. B **106**, 054423 (2022).

[40] D. Dahlbom, C. Miles, H. Zhang, C. D. Batista, and K. Barros, Phys. Rev. B **106**, 235154 (2022).

[41] C. Miles, K. Barros, M. Wilson, D. Dahlbom, S. Quinn, H. Zhang, and S. Matin, SunnySuite, https://Github.Com/SunnySuite/Sunny.Jl (2022).

[42] https://wrap.warwick.ac.uk/143674.

[43] SMART: v.5.630, Bruker Molecular Analysis Research Tool (Bruker AXS, Madison, 2002).

[44] G. M. Sheldrick, CELL_NOW (Georg-August-Universität, Göttingen, 2002).

[45] SAINTPLUS: v.6.45a, Data Reduction and Correction Program (Bruker AXS, Madison, 2001).

[46] G. M. Sheldrick, TWINABS: v.1.05, an Empirical Absorption Correction Program (Bruker AXS Inc., Madison, 2002).

[47] SHELXTL: v.6.14, Structure Determination Software Suite (Bruker AXS Inc., Madison, WI, 2003).

[48] J. C. Lashley, M. F. Hundley, A. Migliori, J. L. Sarrao, P. G. Pagliuso, T. W. Darling, M. Jaime, J. C. Cooley, W. L. Hults, L. Morales *et al.*, Cryogenics (Guildf). **43**, 369 (2003).

[49] S. J. Blundell, Contemp. Phys. **40**, 175 (1999).

[50] L. C. Chapon, P. Manuel, P. G. Radaelli, C. Benson, L. Perrott, S. Ansell, N. J. Rhodes, D. Raspino, D. Duxbury, E. Spill *et al.*, Neutron News **22**, 22 (2011).

[51] J. Rodríguez-Carvajal, Phys. B: Condens. Matter **192**, 55 (1993).

[52] G. Kresse and J. Furthmüller, Comput. Mater. Sci. **6**, 15 (1996).

[53] G. Kresse and J. Furthmüller, Phys. Rev. B **54**, 11169 (1996).

[54] J. P. Perdew, K. Burke, and M. Ernzerhof, Phys. Rev. Lett. **77**, 3865 (1996).

[55] G. Kresse and D. Joubert, Phys. Rev. B **59**, 1758 (1999).

[56] P. E. Blöchl, Phys. Rev. B **50**, 17953 (1994).

[57] G. Ehlers, A. A. Podlesnyak, and A. I. Kolesnikov, Rev. Sci. Instrum. **87**, 093902 (2016).

[58] G. Ehlers, A. A. Podlesnyak, J. L. Niedziela, E. B. Iverson, and P. E. Sokol, Rev. Sci. Instrum. **82**, 085108 (2011).

[59] S. E. Hahn, R. S. Fishman, and G. Ehlers, https://github.com/SpinWaveGenie/SpinWaveGenie (2019).

[60] T. Masuda, I. Tsukada, K. Uchinokura, R. Coldea, M. Kenzelmann, A. Zheludev, S. Raymond, E. Ressouche, P. Böni, and K. Kakurai, Phys. Rev. B **64**, 054422 (2001).

[61] J. Kokalj, J. Herbrych, A. Zheludev, and P. Prelovšek, Phys. Rev. B **91**, 155147 (2015).

[62] S. R. White, Phys. Rev. B **72**, 180403 (2005).

[63] U. Schollwöck, Rev. Mod. Phys. **77**, 259 (2005).

[64] G. Alvarez, Comput. Phys. Commun. **180**, 1572 (2009).

[65] DMRG++, https://G1257.Github.Io/DmrgPlusPlus/.

[66] A. Nocera and G. Alvarez, Phys. Rev. E **94**, 053308 (2016).

[67] P. A. Goddard, J. Singleton, A. L. Lima Sharma, E. Morosan, S. J. Blundell, S. L. Bud'ko, and P. C. Canfield, Phys. Rev. B **75**, 094426 (2007).

[68] J. Detwiler, G. Schmiedeshoff, N. Harrison, and A. Lacerda, Phys. Rev. B **61**, 402 (2000).

[69] L. Noodleman, J. Chem. Phys. **74**, 5737 (1981).

[70] F. Neese, ORCA v.2.8, Revision 2131 (Institut für Physikalische und Theoretische Chemie, Bonn, 2010).

[71] F. Neese, Coord. Chem. Rev. **253**, 526 (2009).

[72] S. Sinnecker, F. Neese, and W. Lubitz, J. Biol. Inorg. Chem. **10**, 231 (2005).

[73] K. Yamaguchi, Y. Takahara, and T. Fueno, in *Appl. Quantum Chem.*, edited by V. H. Smith, H. F. Schafer III, and K. Morokuma (D. Reidel, Boston, 1986), p. 155.

[74] T. Soda, Y. Kitagawa, T. Onishi, Y. Takano, Y. Shigeta, H. Nagao, Y. Yoshioka, and K. Yamaguchi, Chem. Phys. Lett. **319**, 223 (2000).

[75] A. Schäfer, H. Horn, and R. Ahlrichs, J. Chem. Phys. **97**, 2571 (1992).